

## Smooth contact strategies with emphasis on the modeling of balloon angioplasty with stenting

D. E. Kiousis<sup>1</sup>, T. C. Gasser<sup>2</sup> and G. A. Holzapfel<sup>1,2,\*</sup>,<sup>†</sup>

<sup>1</sup>*Institute for Biomechanics, Graz University of Technology, Kronesgasse 5, 8010 Graz, Austria*

<sup>2</sup>*Department of Solid Mechanics, School of Engineering Sciences, Royal Institute of Technology (KTH), Osquars Backe 1, 100 44 Stockholm, Sweden*

### SUMMARY

Critical to the simulation of balloon angioplasty is the modeling of the contact between the artery wall and the medical devices. In standard approaches, the 3D contact surfaces are described by means of  $C^0$ -continuous facet-based techniques, which may lead to numerical problems. This work introduces a novel contact algorithm where the target surfaces are described by polynomial expressions with  $C^2$ -continuity. On the basis of uniform cubic B-splines, two different parametrization techniques are presented and compared, while the related implementation of the algorithm into a finite element analysis program is described. Two numerical examples are selected to demonstrate the special merits of the proposed contact formulation. The first example is a benchmark contact problem selected to point out the special features of the proposed strategies. The second example is concerned with the simulation of balloon angioplasty and stenting, where the contact between the balloon, the stent and the artery wall is numerically modeled. A patient-specific 3D model of a stenotic femoral artery serves as a basis. The study concludes by identifying the changes in the mechanical environment of the artery in terms of contact forces and strains by considering two different stent designs. Copyright © 2008 John Wiley & Sons, Ltd.

Received 22 January 2007; Revised 5 November 2007; Accepted 18 November 2007

KEY WORDS: contact mechanics; smooth surfaces; B-spline; balloon angioplasty; stent

### 1. INTRODUCTION

Balloon angioplasty with or without stenting is an interventional clinical treatment aiming at the dilation of stenotic arteries in order to increase the blood flow through the artery. Its steadily growing medical, economical and scientific interests (see [1]) have motivated clinical and biomechanical communities to a considerable research effort. An increasing number of computational studies, by means of numerical tools such as the finite element method, has been noted during the past

\*Correspondence to: G. A. Holzapfel, Institute for Biomechanics, Graz University of Technology, Kronesgasse 5-I, A-8010 Graz, Austria.

<sup>†</sup>E-mail: holzapfel@tugraz.at

decades. A common target of all the presented works is the detailed understanding of the underlying mechanisms, the optimization of the interventional protocols, and finally, the improvement in the clinical outcome.

Especially for the engineering community, the modeling and analysis of stent dilation in an artery turns out to be of great interest. It involves a number of challenging areas within computational mechanics such as non-linear continuum mechanics and the development of non-linear and anisotropic constitutive laws. However, most critical to a reliable modeling of the stenting procedure is the contact mechanics formulation. The stenting technique involves three different contact problems (balloon–stent, stent–artery and balloon–artery); thus, a robust and stable contact algorithm should be used in order to successfully and efficiently address the problem.

For the finite element analysis of contact problems, various methods are applied to incorporate the contact constraints in the variational formulation (details are provided in [2, 3]). However, the often encountered choice of  $C^0$ -continuous descriptions for the arbitrarily curved contact interfaces may lead to numerical instabilities. These instabilities arise from the sliding of contractor nodes over target facet boundaries, where a jump of the normal vector occurs, and the assumption of smoothness is violated [4]. This discontinuity of the normal vector usually leads to rough non-physical behavior, oscillation of contact forces, numerical instabilities and loss of the quadratic convergence rate. This is especially the case when highly curved surfaces of engineering or biological structures, such as blood vessel walls, are modeled. One possible remedy that addresses the above-mentioned problems is the use of a disproportionately fine mesh in the vicinity of the contact regions. Such an attempt could lead to high computational costs and is for this reason considered to be inefficient and is often avoided. Hence, the need for special algorithmic treatment is implied.

Towards this direction, higher-order parametrizations have recently been derived with the aim of describing one of the contact surfaces, allowing thus smooth sliding of the nodes on the contact interface. Through this approach, the discontinuities induced by spatial discretizations can be avoided and the numerical outcome can be improved. Among the most common smooth parametrizations used in conjunction with contact algorithms are the cubic Hermite interpolations [5, 6], the cubic B-splines [7], the Overhauser splines [8, 9] and NURBS [10, 11]. The more recent publication [12] makes use of a more advanced smooth parametrization, i.e. subdivision surfaces, which was first introduced in [13] and originates from the computer-aided design community. All the previously mentioned smooth discretizations have been successfully applied to a series of engineering contact problems, exploiting significant advantages over facet-based approaches [14, 11]. Therefore, the use of at least  $C^1$ -continuous interpolation schemes in the modeling of the contact-dominated stenting procedure is also appreciated. In this way, stability problems that are present in typical simulations of cardiovascular intervention (see [15]) could be avoided.

A detailed study of the literature reveals a large number of papers that attempt to model numerically the stent expansion in atherosclerotic arteries. Despite the promising scientific outcomes of these papers, the majority consider cylindrical arterial geometries [16–21]. More refined patient-specific models are included in [22, 23], while the balloon catheter and its contact with the artery wall are not modeled. This is also the case for the above-cited papers. To the authors' knowledge, the recent article [24] is the first that presents a finite element computation of the contact interaction between the balloon, the stent and the arterial wall. Nevertheless, a cylindrical model for the artery was used again.

This study aims at proposing an innovative 3D contact algorithm that uses  $C^2$ -continuous parametrizations for the description of the target surfaces of the involved contacting bodies. In

particular, two different polynomial functions are investigated. We employ the uniform cubic B-splines [25–27] that have been used previously in computer design, in aerospace and in the automotive industry. Then we present a novel modification of the fourth-order B-spline polynomials, which, with no significant computational cost, manages to additionally interpolate the points of the control net. Thus, a more precise approximation of the geometric models can be achieved. The smooth contact approach is implemented into the multi-purpose finite element analysis program (FEAP) [28]. The necessary implementation steps are provided in detail. The developed numerical tool is applied to a classical contact mechanics problem, often encountered in the literature [14, 29]. The example involves finite deformations and large sliding, and the acquired results (in the form of contact forces) point out the robustness of the contact algorithm and the features of the selected parametrizations.

As a second example, we present a 3D simulation of stenting. It investigates one stenosis that is located in a human femoral artery. The geometric model of the arterial wall is obtained from high-resolution magnetic resonance imaging (hrMRI) and is re-constructed by means of NURBS [30]. The vessel is modeled as a homogeneous, isotropic material, exposing a non-linear behavior at higher strains. Uniaxial tensile tests of femoral artery tissues are used to establish the constitutive law and the associated material parameters. A novel, cylindrically orthotropic material model is developed in order to capture the realistic behavior of the balloon catheter. To the authors' knowledge, it appears that no model considers yet the 3D, non-axisymmetrical geometries and contact interactions between the three continua. In addition, the approach documented in this paper is, along with [31], one of the first attempts to employ specific contact algorithmic treatments to the demanding simulation of balloon angioplasty and stenting. The final target of the work is to predict the outcome of the treatment for two different stent configurations. More specifically, the development of mechanical strains and contact forces on the inner arterial wall during and after the expansion of the stents is studied.

This paper is organized as follows: Section 2 briefly reviews the governing equations and the variational formulation for frictionless contact problems. In Section 3, the two parametrization schemes, which are applied for the representation of the contact surfaces, are introduced and discussed. Section 4 describes the implementation aspects of the developed smooth contact techniques into a finite element framework. The performance of the discussed smoothing algorithms is outlined in Section 5 by means of two numerically demanding contact problems. Finally, in Section 6, concluding remarks are provided and the limitations of the proposed approach are discussed.

## 2. CONTACT KINEMATICS

A sufficient way to model contact problems involving large deformations is the finite strain approach in conjunction with the target–contractor concept. Without loss of generality, two bodies  $\mathcal{B}^\alpha$ ,  $\alpha = m, s$ , are considered, approaching each other during a finite deformation process and coming into contact on parts of their boundaries, denoted by  $\Gamma_c^\alpha$  (see Figure 1). Each of the two continua occupies the bounded domain  $\Omega^\alpha \subset \mathbb{R}^\zeta$ , where  $\zeta$  denotes the number of space dimensions of the problem. The target (or master) body is denoted by  $\mathcal{B}^m$ , and the contractor (or slave) body is denoted by  $\mathcal{B}^s$ . The boundary  $\Gamma^\alpha$  of  $\mathcal{B}^\alpha$  consists of three parts  $\Gamma_\sigma^\alpha$ ,  $\Gamma_u^\alpha$  and  $\Gamma_c^\alpha$ , so that  $\partial\Omega^\alpha = \Gamma_\sigma^\alpha \cup \Gamma_u^\alpha \cup \Gamma_c^\alpha$ , where von Neumann, Dirichlet and contact boundary conditions are prescribed, respectively. The spatial points of the current configuration are denoted by  $\mathbf{x}^\alpha$ .

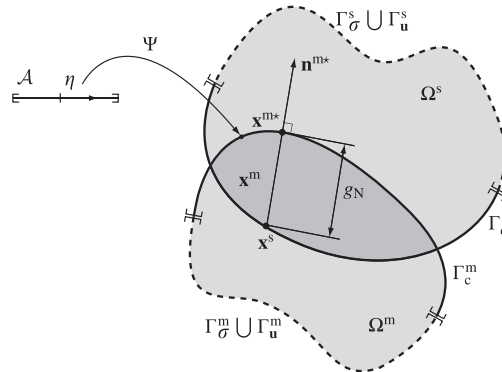


Figure 1. The 2D representation of the deformed configuration of two contact bodies  $\mathcal{B}^2$  and definition of the closest point projection.

In order to specify the contact constraints, it is useful to introduce the mapping  $\Psi: \mathcal{A} \rightarrow \mathbb{R}^{\zeta-1}$  so that  $\mathbf{x}^m = \Psi(\zeta, \eta)$ , where  $\zeta$  and  $\eta$  are the convective coordinates of the parameter plane  $\mathcal{A}$ . The derivation of the governing equations, discussed next, follows closely the approaches documented in [32, 33].

2.1. Normal contact of 3D bodies

Every point  $\mathbf{x}^s$  on  $\Gamma^s$  can be associated with a point  $\mathbf{x}^{m*} = \mathbf{x}^m(\zeta^*, \eta^*)$  via the minimum distance problem

$$d(\zeta, \eta) = \|\mathbf{x}^s - \mathbf{x}^{m*}\| = \min_{\mathbf{x}^m \in \Gamma_c^m} \|\mathbf{x}^s - \mathbf{x}^m(\zeta, \eta)\| \tag{1}$$

The solution to (1), hence the target point  $\mathbf{x}^{m*}$ , is the orthogonal projection of the contractor point  $\mathbf{x}^s$  onto the current target surface  $\Gamma_c^m$ , as shown in Figure 1. The minimum distance problem can be solved using a local Newton iteration algorithm of the form

$$\xi_{i+1}^* = \xi_i^* - \frac{\frac{\partial d}{\partial \xi}}{\frac{\partial^2 d}{\partial \xi^2}} \bigg|_{\xi = \xi_i^*} \tag{2}$$

where the solution vector  $\xi^*$  stands for the set of the convective coordinates  $(\zeta^*, \eta^*)$ , which is not always unique. Once the point  $\mathbf{x}^{m*}$  is known, a gap function  $g_N$  can be defined as

$$g_N = (\mathbf{x}^s - \mathbf{x}^{m*}) \cdot \mathbf{n}^{m*} \tag{3}$$

where  $\mathbf{n}^{m*}$  is the outward unit normal on the target surface at the target point  $\mathbf{x}^{m*}$  (see Figure 1). The gap function  $g_N$  defines the state of normal contact. The conditions upon admissibility of  $\mathbf{x}^s$

are summarized in the Karush–Kuhn–Tucker conditions

$$g_N \geq 0, \quad t_N \leq 0, \quad t_N g_N = 0 \quad (4)$$

where  $t_N$  is associated with the contact force  $\mathbf{t}$  via  $\mathbf{t} = t_N \mathbf{n}$  for the case of frictionless contact. The three relations in (4) represent conditions for impenetrability, compressive normal interaction and complementarity of gap and contact pressure, respectively.

## 2.2. Variational formulation

In order to obtain solutions to the frictionless contact problem, a finite element framework is developed, which treats normal contact as a unilateral constraint problem. In this case, the normal contact pressure is not computed from a constitutive equation but can be deduced from the constraint equations. The latter can be incorporated into the formulation through the virtual work contributions due to contact.

The virtual work statement for the interacting bodies is described by the relation

$$\sum_{\alpha=m,s} \delta W_{\text{ext}}^\alpha + \sum_{\alpha=m,s} \delta W_{\text{ext,c}}^\alpha = \sum_{\alpha=m,s} \delta W_{\text{int}}^\alpha \quad (5)$$

The contact contribution of the two bodies to the external virtual work is

$$\sum_{\alpha=m,s} \delta W_{\text{ext,c}}^\alpha = \int_{\Gamma_c^s} \mathbf{t}^s \cdot \delta \mathbf{u}^s \, d\Gamma_c^s + \int_{\Gamma_c^m} \mathbf{t}^m \cdot \delta \mathbf{u}^m \, d\Gamma_c^m \quad (6)$$

where  $\mathbf{u}^\alpha$  denotes the prescribed displacement field. The balance of linear momentum implies that the differential contact force exerted on  $\mathcal{B}^m$  is equal and opposite to the force on the body  $\mathcal{B}^s$  everywhere on  $\Gamma_c^\alpha$ ,  $\alpha = m, s$ ; therefore,  $\mathbf{t}^s = -\mathbf{t}^m = \mathbf{t}$ . Equation (6) then deduces into

$$\sum_{\alpha=m,s} \delta W_{\text{ext,c}}^\alpha = \int_{\Gamma_c^s} \mathbf{t} \cdot [\delta \mathbf{u}^s - \delta \mathbf{u}^m(\xi, \eta)] \, d\Gamma_c^s \quad (7)$$

Since  $\mathbf{t} = t_N \mathbf{n}$ , the expression  $\mathbf{n} \cdot [\delta \mathbf{u}^s - \delta \mathbf{u}^m(\xi, \eta)]$  can be derived, which is equal to  $\delta g_N$ . Thus, (7) yields

$$\sum_{\alpha=m,s} \delta W_{\text{ext,c}}^\alpha = \int_{\Gamma_c^s} t_N \delta g_N \, d\Gamma_c^s \quad (8)$$

The conditions described in (4)<sub>1,2</sub> state an inequality variational principle. Therefore, a regularization technique is required. The one chosen here is the penalty method. Then, for normal contact, the Karush–Kuhn–Tucker conditions are replaced by the expression  $\varepsilon_N \langle g_N \rangle$ , where  $\langle \cdot \rangle$  denotes the Macauley bracket representing the positive part of its argument, and  $\varepsilon_N$  is the normal penalty parameter. The advantage of the penalty method (more than its simplicity) is that it evaluates the contact pressure in a displacement-driven way since it associates the contact force only with the penetration  $g_N$ . However, it must be mentioned that the solution to the penalty method is recovered from the above formulation for  $\varepsilon_N \rightarrow \infty$ . Too high penalizations, though, can lead to ill-conditioning of the system of equations.

Next, to incorporate the contact contributions, as described in (8), into the finite element procedure, the associated residual vector  $[\mathbf{f}_c]$  and the stiffness matrix  $[\mathbf{K}_c]$ , i.e.

$$[\mathbf{f}_c]_i = \varepsilon_N g_N \left( \frac{\partial g_N}{\partial [\mathbf{u}]_i} \right), \quad [\mathbf{K}_c]_{ij} = \varepsilon_N \frac{\partial}{\partial [\mathbf{u}]_j} \left( g_N \frac{\partial g_N}{\partial [\mathbf{u}]_i} \right) \quad (9)$$

have to be evaluated for  $i, j = 1, \dots, w$ , respectively, where  $w$  is the total number of the involved nodes (contractor node and the nodes of the target surface). For example, in the 3D case of spatial discretizations,  $w = 5$ , whereas when a smooth target surfaces is considered, defined by a control polyhedron consisting of  $r \times r$  target nodes, the total number of nodes of the contact partners is  $w = (r^2 + 1)$ . The derivation of the matrix formulae described in Equations (9) is presented in detail in Section 4.3.

### 3. SMOOTH SURFACE DISCRETIZATIONS FOR CONTACT PROBLEMS

As mentioned in the Introduction, the observed non-continuity of the normal vector due to spatial discretizations of the master contact surface may lead to numerical instabilities. A solution that addresses efficiently the problem is the approximation of the contact surfaces by means of higher-order parametrizations. In this section, two  $C^2$ -continuous functions are discussed. The first employed parametrization is the uniform cubic B-splines. The second parametrization is a new technique, developed in the context of the present work. It is based on B-splines but provides a closer approximation of the contacting bodies' geometry.

#### 3.1. Cubic B-spline surfaces

B-splines have been extensively used in the aerospace and automotive industries during the past 30 years, and they are a powerful tool for the design of free form curves or surfaces [25–27]. In particular, uniform cubic B-spline surfaces (spline order  $n = 4$ ) are defined over a bidirectional net of 16 control points  $\mathbf{P}_{i,j}$ ,  $i, j = 1, \dots, 4$ , which may be characterized by the tensor product

$$\mathbf{S}(u, v) = \sum_{i=1}^4 \sum_{j=1}^4 B_i(u) B_j(v) \mathbf{P}_{i,j}, \quad 0 \leq u, v \leq 1 \quad (10)$$

where  $B_i(t)$ ,  $i = 1, \dots, 4$ , are the cubic basis functions

$$\begin{aligned} B_1(t) &= \frac{1}{6}(1 - 3t + 3t^2 - t^3) \\ B_2(t) &= \frac{1}{6}(4 - 6t^2 + 3t^3) \\ B_3(t) &= \frac{1}{6}(1 + 3t + 3t^2 - 3t^3) \\ B_4(t) &= \frac{1}{6}t^3 \end{aligned} \quad (11)$$

and  $t$  stands for either parameter  $u$  or  $v$ .

Figure 2(a) shows an example of a  $4 \times 4$  control mesh and its corresponding uniform cubic B-spline surface  $\mathbf{S}$ , computed and plotted in MATHEMATICA [34]. In Figure 2(b), two overlapping control polyhedrons and two adjacent uniform cubic B-spline surfaces ( $\mathbf{S}_1$  and  $\mathbf{S}_2$ ) are shown. In the same figure, the  $C^1$ -continuous border between the two surfaces is also graphically represented.

Among the main properties of cubic B-splines, two are of particular interest for contact algorithms. Cubic B-splines have *second degree* ( $C^2$ -) *continuity*, meaning that  $\mathbf{S}$  (Equation (10)) is twice continuously differentiable. This, as mentioned in [11], is a necessary requirement for quadratic rate of convergence within non-linear solution schemes. Owing to the higher-order

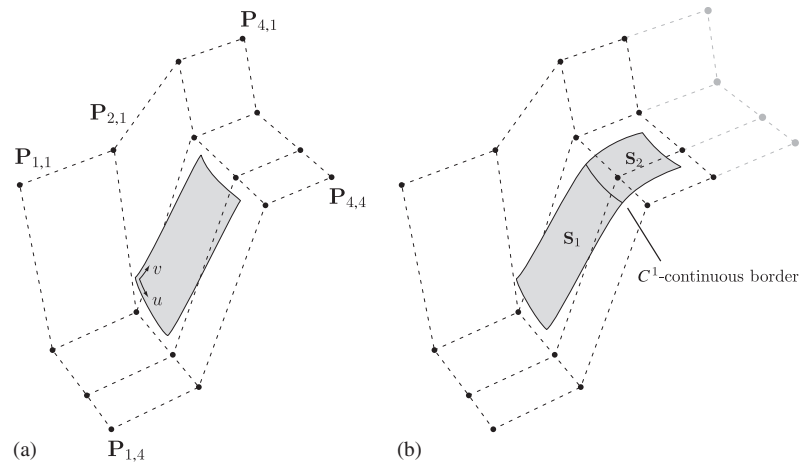


Figure 2. Uniform cubic B-spline surfaces: (a)  $4 \times 4$  control mesh and its corresponding uniform cubic B-spline surface and (b) example of two overlapping control grids and two adjacent cubic B-spline surfaces, where  $C^1$ -continuity property of the surfaces is pointed out.

continuity of B-splines, the normal vector on the surface is uniquely and continuously defined. Furthermore, B-splines offer *local support* that enables the definition of a region of influence for a particular control point on the surface.

### 3.2. Modified uniform cubic B-spline surfaces

Besides the useful properties of B-splines, one inherent disadvantage of the parametrization is that it cannot represent surfaces with arbitrary mesh topology, thus being restricted to surfaces described by quadrilateral structured meshes. This problem can be overcome through several approaches such as Gregory patches [35], subdivision schemes [13] or other polynomial expressions [36, 37] (these techniques are not addressed in this paper though). In addition, B-spline surfaces do not necessarily interpolate any of their control points (refer to the literature cited previously). This is clearly shown in Figures 2(a) and (b). During the last years, several methods (based mainly on splines) have been developed in order to model biological structures more effectively and more smoothly (for example, joints and femurs). Among the most promising works are [36, 38, 39], where polynomial functions are fitted to random surface points. These approaches remove the need for structured control meshes and provide sufficient and more accurate smoothing of the surface data.

With this in mind, a new parametrization is proposed here. It is based on the uniform cubic B-splines (Equation (10)), enhanced by one more polynomial function in order to interpolate the four central vertices of the control grid. The mathematical expression of this new parametrization, which we subsequently call *modified* uniform cubic B-splines and denote by  $\mathbf{S}'$ , is

$$\mathbf{S}'(u, v) = \sum_{i=1}^4 \sum_{j=1}^4 B_i(u) B_j(v) \mathbf{P}_{i,j} + \sum_{i=1}^4 N_i(u, v) \mathbf{U}_i, \quad 0 \leq u, v \leq 1 \quad (12)$$

The term  $\sum_{i=1}^4 N_i(u, v) \mathbf{U}_i$  in (12) is the sum of the product of a set of basis functions  $N_i(u, v)$ ,  $i = 1, \dots, 4$ , based on the trigonometric functions, and is defined as

$$\begin{aligned} N_1(u, v) &= \frac{1}{4}(1 + \cos(\pi u))(1 + \cos(\pi v)) \\ N_2(u, v) &= \frac{1}{4}(1 - \cos(\pi u))(1 + \cos(\pi v)) \\ N_3(u, v) &= \frac{1}{4}(1 - \cos(\pi u))(1 - \cos(\pi v)) \\ N_4(u, v) &= \frac{1}{4}(1 + \cos(\pi u))(1 - \cos(\pi v)) \end{aligned} \quad (13)$$

with the displacement vectors  $\mathbf{U}_i$ ,  $i = 1, \dots, 4$ . An example of the modified cubic B-splines is presented in Figure 3(a), in which it can be seen that the new surface  $\mathbf{S}'$  interpolates the four inner points of its control mesh. In the same figure, the ‘original’ cubic B-spline surface is plotted and the definition of the displacement vector  $\mathbf{U}_3$  is shown. In more detail, the displacement vectors are given as the distance between the edges of the uniform cubic B-spline surface and the (inner) four corresponding control points according to

$$\begin{aligned} \mathbf{U}_1 &= \mathbf{P}_{2,2} - \mathbf{S}(0, 0) \\ \mathbf{U}_2 &= \mathbf{P}_{2,3} - \mathbf{S}(1, 0) \\ \mathbf{U}_3 &= \mathbf{P}_{3,3} - \mathbf{S}(1, 1) \\ \mathbf{U}_4 &= \mathbf{P}_{3,2} - \mathbf{S}(0, 1) \end{aligned} \quad (14)$$

A similar approach to the one proposed here is given in [37], where a parametric polynomial and the Fourier series functions are superimposed to form a new parametrization technique. Through this method, the authors claim smoother results for the swine femoral surface when compared with

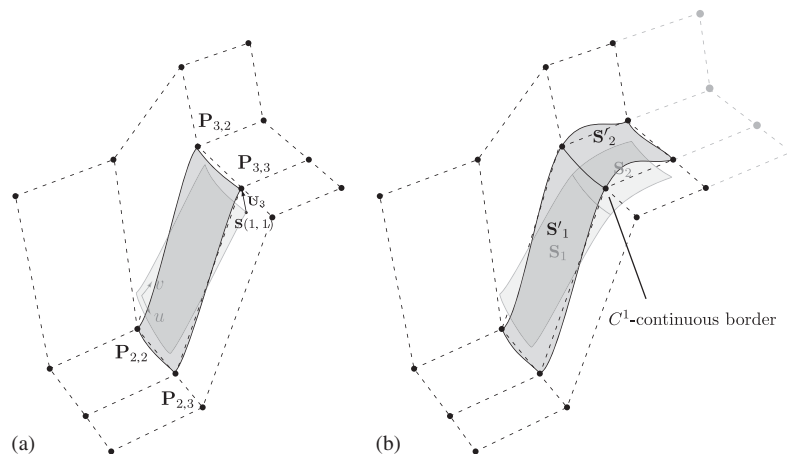


Figure 3. Modified uniform cubic B-splines: (a)  $4 \times 4$  control mesh, the ‘original’ uniform cubic B-spline surface  $\mathbf{S}$  and its modification  $\mathbf{S}'$  that passes through the four inner nodes of the control polyhedron. The definition of the displacement vector  $\mathbf{U}_3$  is also shown and (b) two adjacent ‘original’ uniform cubic B-spline surfaces  $\mathbf{S}_1$  and  $\mathbf{S}_2$ , and the generated modified surfaces  $\mathbf{S}'_1$  and  $\mathbf{S}'_2$ .

B-splines alone. Additionally, the superposition of the two functions does not tend to smoothen localized undulations and can model complex surfaces with ripples.

As can be seen, the newly introduced part of relation (12) is infinitely continuously differentiable due to the trigonometric nature of the basis functions  $N_i(u, v)$ ,  $i = 1, \dots, 4$ , i.e. Equation (13). Therefore, the modified expression of the uniform cubic B-spline surfaces retains the property of the  $C^2$ -continuity and the continuous definition of the normal vector along them. In addition, the basis functions  $N$  have the properties of non-negativity, partition of unity and local support, but the modified cubic B-spline surfaces do not have the geometric characteristic of the strong convex hull property.

In Figure 3(b), the  $C^1$ -continuous border between two adjacent modified uniform cubic B-spline surfaces ( $S'_1$  and  $S'_2$ ) is pointed out. The same figure also indicates that even though one modified surface passes through only four nodes of the control mesh, the consideration of overlapping control polyhedrons leads to the interpolation of all points, hence, of all superficial nodes of a finite element mesh.

One of the advantages of the parametrization described in Equation (12) is its simplicity. No fitting is required and thus no additional linear systems have to be solved, as in other approaches [36, 38, 39]. In complex 3D contact problems, computational cost is an important aspect that should be by all means taken into consideration. The modified cubic B-splines are to this extent a faster and more straightforward parametrization tool, able to accurately interpolate the nodes of the control grid. A closer observation of Figure 3 (and Figure 8 given later) shows, however, one drawback of the new parametrization. When abrupt curvature changes take place within short distances, the parametrization leads to local waviness. This behavior derives from the requirement of the surface to pass through the control net, which is not usually the case for the more thorough approaches cited above. On the other hand, however, the number of oscillations should be limited since the  $C^2$ -continuous surface is not required to fit a large amount of scarcely positioned image data points, but a comparatively smaller and smoother set of finite element nodes. One should also note that it is this property that, at the same time, allows modified B-splines to represent surfaces with possible undulations or ripples. The features of the new parametrization technique are further discussed in Section 5.1.

#### 4. IMPLEMENTATION STRATEGIES

One of the most demanding and at the same time most challenging tasks of this work is the incorporation of the smooth parametrization techniques into a finite element framework. For the development of a contact algorithm based on smooth parametrizations, the following four major points should be taken into consideration:

- (i) the evaluation of the interpolation functions and, consequently, of the smooth target contact surfaces,
- (ii) the identification of the contact pairs,
- (iii) the calculation of the contact contributions and
- (iv) the assembling of the contact elements' residuum and stiffness into the global residuum vector and stiffness matrix.

The open-source program FEAP [28] provides the possibility for the implementation of such a numerical scheme and it is, therefore, chosen as the basis for the developed contact algorithm. The

additional needs are met by a series of subroutines, forming the user contact driver *SmooC* (standing for *Smooth Contact*), which communicates with FEAP through user-defined macro commands. All implementation steps are discussed in the following section.

#### 4.1. Implementation of the smooth interpolation schemes

As already mentioned in Section 3, each uniform cubic (and modified) B-spline surface is defined by a structured mesh of control points,  $\mathbf{P}_{i,j}$ ,  $i, j = 1, \dots, 4$ , see Equations (10) and (12). Thus, the evaluation of the smooth surface  $\mathbf{S}_k$  associated with a specific facet  $\mathbf{q}_k$  of the discretized target contact surfaces requires initially the definition of a  $4 \times 4$  control polyhedron. In the context of this work, each control grid is formed by the nodes of the considered facet  $\mathbf{q}_k$  as well as by the nodes of its neighbor facets that are located on the contact surface, as in the two examples of facets  $\mathbf{q}_a$  and  $\mathbf{q}_b$  shown in Figure 4. This is a significant advantage of the proposed approach since it allows one to base the geometrical modeling and the finite element analysis on an identical representation paradigm. Such a unified framework yields a robust interface between geometric design and mechanical analysis, as discussed in [40, 41]. The structured control patch consists of 16 nodes for each contact facet, subsequently denoted by  $\mathbf{q}_k^{\text{cp}}$ . This ingredient, hence the control polyhedron for each facet of the master surfaces, is provided by *SmooC*, and more specifically by the macro *CPoin*, executed before the beginning of the computation. The macro reads the mesh coordinates and connectivity list, identifies the adjacent facets of each facet  $\mathbf{q}_k$  belonging to the target surfaces and generates the structured, control point patches  $\mathbf{q}_k^{\text{cp}}$ .

After acquiring the control polyhedrons  $\mathbf{q}_k^{\text{cp}}$ , the parametrization of every contact facet by the interpolation functions, described in Equations (10) and (12), is straightforward. The smooth surface  $\mathbf{S}_k(u, v)$  for each facet is computed using a self-programmed MATHEMATICA-generated

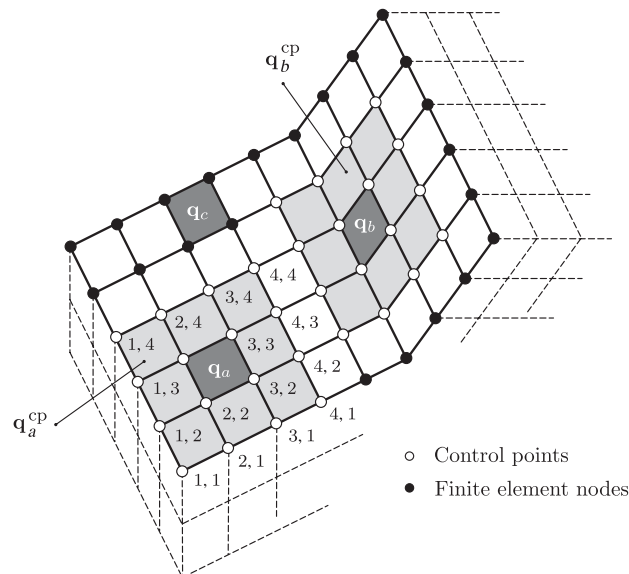


Figure 4. Discretized arbitrary master contact body: the control polyhedrons that define the smooth interpolations of two different master contact facets ( $\mathbf{q}_a$ ,  $\mathbf{q}_b$ ) are shown.

function, called by the macro `MSurf`. The required inputs of `MSurf` are the obtained control polyhedrons  $\mathbf{q}^{\text{CP}}$  as well as the contractor nodes  $\mathbf{x}^s$ . The same macro performs a series of further operations, defined by an index, which are discussed in the following paragraphs.

#### 4.2. Contact search

The algorithms for detecting contact are of utmost importance since the time for the definition of the possible contact bodies and contact pairs could dominate the overall cost of the numerical simulation. Therefore, although search algorithms are not the main focus of this paper, an attempt is made to tackle the search problem by means of refined and time-efficient methods.

In this work, no global search is taken into consideration. The possible contact bodies are predefined and hence are considered as an input of the contact problem. In other words, only local search algorithms are addressed, where two bodies are in contact but it is not clear which contractor node contacts which target segment. There are several possibilities of dealing with this problem. The approach followed here splits the detection of local contact for a given contractor node  $\mathbf{x}^s$  into two different phases.

Initially, the set of the closest target facets  $\mathbf{q}_k$  for the contractor node  $\mathbf{x}^s$  is identified. This can be performed by defining a search radius  $r_{\text{search}}$ , which is related to the problem and highly dependent on the discretization size of the target contact surfaces. In the case where  $\|\mathbf{x}^s - \mathbf{x}_{k,\text{mid}}^m\| \leq r_{\text{search}}$ , where  $\mathbf{x}_{k,\text{mid}}^m$  is the middle point of the facet  $\mathbf{q}_k$ , the target facet  $\mathbf{q}_k$  is considered as a part of the set mentioned above. The purpose of this step is to limit the number of contact search iterations and, consequently, their computational time.

In the second step, the parametrization of the closest target facets is carried out by application of (10) or (12), and the minimum distance problem (depicted in (1)) is solved; the smooth surface  $\mathbf{S}_k^*$  that contains the orthogonal projection  $\mathbf{x}^{m*}$  is obtained. The first part of this step is local in nature and for this reason not computationally expensive, whereas the minimum distance problem does not have a closed-form solution. Therefore, a Newton algorithm has to be applied, see (2). In order to further limit the computational time, a better initialization of the Newton algorithm is required. This is achieved by generating an equally divided mesh of the smooth surface and by considering the mesh point that is closer to the contractor node  $\mathbf{x}^s$  as an initial guess of the iteration procedure. The evaluation of  $\mathbf{x}^{m*}$  is followed by the computation of the gap function  $g_N$ . If the Karush–Kuhn–Tucker conditions are violated, i.e. Equation (4), then the pair  $\mathbf{x}^s - \mathbf{S}_k^*$  is considered as in contact. All the above operations are performed by the macro `MSurf`, introduced previously.

#### 4.3. Evaluation and assembling of the contact contributions

The next step after the definition of the contact pairs is the computation of the virtual work contributions due to contact, and more specifically, of the associated contact residual vector  $[\mathbf{f}_c]$  and the stiffness matrix  $[\mathbf{K}_c]$ .

As can be seen from (9), both contact residuum and stiffness depend on the gap function  $g_N$  and on its derivative with respect to the displacements of the associated contractor point and target contact surface. In the approach presented in this paper, the two derivations are carried out on an abstract mathematical level by making use of the `MATHEMATICA` package `ACEGEN` [42]. The same method for contact problems is also applied and documented in References [11, 12].

`ACEGEN` combines several techniques such as the symbolic capabilities of `MATHEMATICA`, automatic differentiation, simultaneous optimization of expressions and stochastic evaluation of

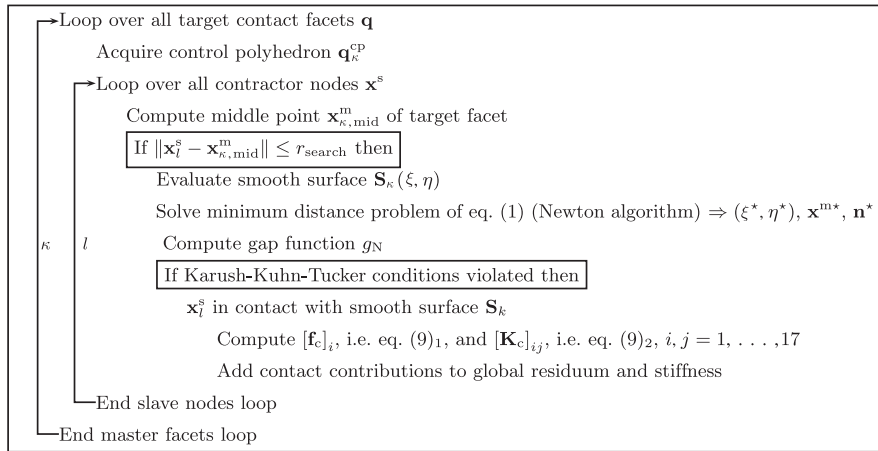


Figure 5. Implementation steps for computing and assembling contact contributions to the residuum and stiffness of an element.

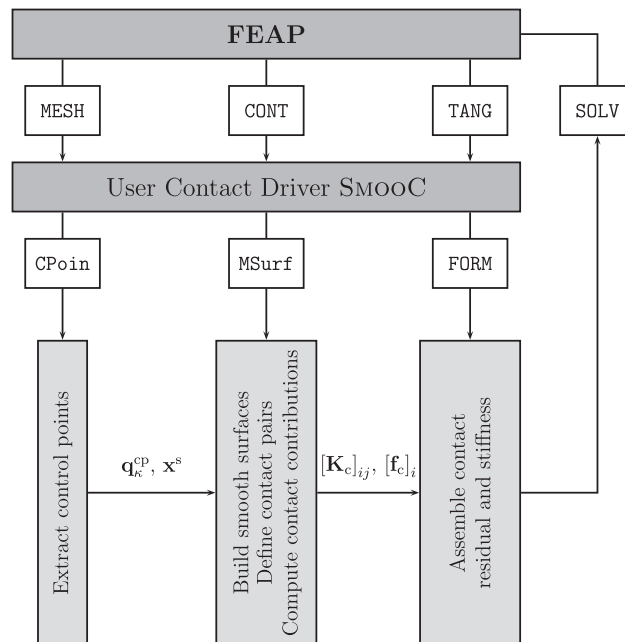


Figure 6. Flowchart of the implementation of the contact algorithm based on  $C^2$ -continuous surfaces into the multi-purpose finite element analysis program (FEAP) [28].

formulas instead of conventional pattern-matching method. The above provides an efficient evaluation method for the non-linear contact quantities which requires less effort compared with manually written codes. The derived symbolic formulae for expressions (9) are computed with MATHEMATICA and translated into an efficient compiled language (Fortran), and the generated subroutine

is implemented into FEAP. The call of this subroutine and the computation of the contact residuum and stiffness are the last functions of the macro command `MSurf`.

When the two described techniques are used for the parametrization of the contact surfaces, the involved nodes in each contact pair are the  $4 \times 4$  control point finite element nodes  $\mathbf{q}_\kappa^{\text{cp}}$  of the smooth target surface and the contractor point  $\mathbf{x}_l^s$ . Therefore, the total degrees of freedom and the number of contact contributions for each contact pair are equal to  $3(4^2 + 1) = 51$ . The obtained results of (9) have to be added to the residuum and the stiffness of the global non-linear system of equations. This operation is performed by the already existing FEAP subroutines `MODPROF` and `CONSTASS`. The first modifies the profile of the residuum and the stiffness by taking into consideration the 51 inputs mentioned above, whereas the second performs the assembling of the residuum vector and the stiffness matrix.

For a better overview, the implementation steps and the flowchart of the developed contact algorithm are summarized in Figures 5 and 6, respectively.

## 5. NUMERICAL EXAMPLES

The features and special merits of the proposed parametrization techniques and of the presented contact approach are demonstrated by means of two numerical examples. Their main aim is to exhibit the numerical robustness of the proposed contact scheme and its ability to numerically treat complex 3D contact problems. Both examples consider contact interactions between incompressible and finite deformable bodies. In the first example, the contact between a brick and a plate is modeled. It is a challenging problem since large sliding is involved. The distribution of the contact forces along the path of the brick is analyzed for the two surface discretizations. The second example is concerned with the numerical simulation of balloon angioplasty with stenting, which, in the field of biomechanics, is a research area of its own. The contact interaction between three different bodies (arterial wall, balloon and stent) is modeled, while a patient-specific 3D geometry of a femoral artery is taken into consideration. The induced contact forces and strains in the arterial wall are discussed in detail.

### 5.1. Brick sliding across a plate

The 3D problem consists of an orthogonal plate and a cubic brick. The dimensions of the plate are  $10\text{mm} \times 20\text{mm} \times 3\text{mm}$  and the brick's edges have a length of 2 mm. The contact interaction of the two bodies is shown in Figure 7(a) and involves the following two steps: (i) the brick is pressed vertically against the plate until it reaches the plate's midplane and (ii) the brick is dragged diagonally along the plate's upper surface.

The material of both bodies is hyperelastic, nearly incompressible and described by the neo-Hookean strain–energy function

$$\Psi = \left( \frac{\kappa}{4} - \frac{\mu}{6} \right) (J^2 - 1 - 2 \ln J) + \frac{\mu}{2} (\bar{I}_1 - 3) \quad (15)$$

The plate is characterized by a bulk modulus of  $\kappa = 1.66 \times 10^3 \text{N/mm}^2$  and a shear modulus of  $\mu = 34 \text{N/mm}^2$ , whereas the brick is characterized by a bulk modulus of  $\kappa = 1.66 \times 10^4 \text{N/mm}^2$  and a shear modulus of  $\mu = 340 \text{N/mm}^2$ . In (15),  $\bar{I}_1 = \text{tr} \bar{\mathbf{C}}$  is the first invariant of the modified

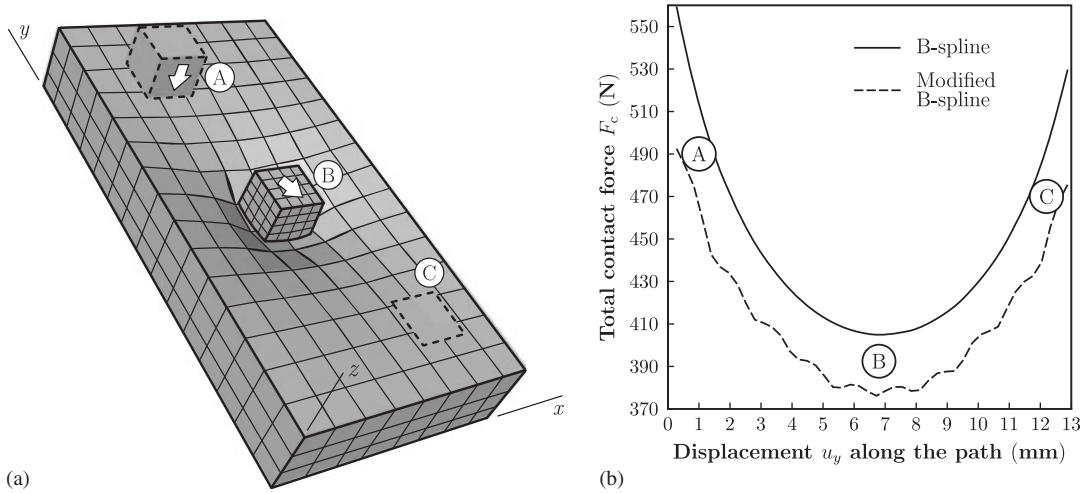


Figure 7. Cubic brick sliding across an orthogonal plate: (a) geometry and finite element mesh of the contacting bodies. Initially, the brick is pressed downwards until it reaches the plate's midplane (A), and then it is dragged diagonally over the plate's upper surface (B) until its final position (C) and (b) distribution of the total contact force along the path of the cubic contractor, computed with the different smooth parametrizations of the target contact surface.

right Cauchy–Green tensor  $\bar{\mathbf{C}} = \bar{\mathbf{F}}^T \bar{\mathbf{F}}$ , where  $\bar{\mathbf{F}} = J^{-1/3} \mathbf{F}$  is the modified deformation gradient with  $J = \det \mathbf{F} > 0$  and  $\det \bar{\mathbf{F}} = 1$ , see [43].

For the discretization of both bodies, relatively coarse meshes are used in order to point out the differences between the used surface parametrizations. More specifically, the finite element computation uses 424 hexahedral elements and 701 nodes, each one has three degrees of freedom. The four peripheral faces of the plate are considered bounded in all three directions. Both loading conditions (pressing and sliding) are applied by means of prescribed displacements on the brick's upper surface, and the complete loading history is applied in 360 time steps (i.e. 360 prescribed displacements).

The upper face of the plate is considered as the target surface, whereas the nodes on the lower face of the brick are the contractor nodes. The target contact surface is discretized by means of the three discussed parametrizations, i.e. (i) planar elements, (ii) uniform cubic B-spline surfaces and (iii) modified uniform cubic B-spline surfaces. The value  $\varepsilon_N = 4500 \text{ N/mm}$  is chosen as the normal penalty parameter and no friction is considered.

The computation is initially performed by making use of the pre-existing FEAP contact scheme that is based on planar elements. In this case, loss of convergence is experienced at the very beginning of the load path (A)–(B) (see Figure 7(a)) and no solution is obtained. As it seems, the main cause of this behavior is that the normal vector jumps when the slave nodes slide over the master elements. This is not the case when the target surface is described by means of the two smooth parametrizations and the developed contact algorithm is used. Then, the non-linear solution scheme converges quadratically and a solution is always achieved.

The contact forces generated during the loading procedure are of special interest since they provide an insight into the contact interaction of the involved bodies and into the used parametrizations of the master contact surface. In Figure 7(b), the contact forces induced on the brick during

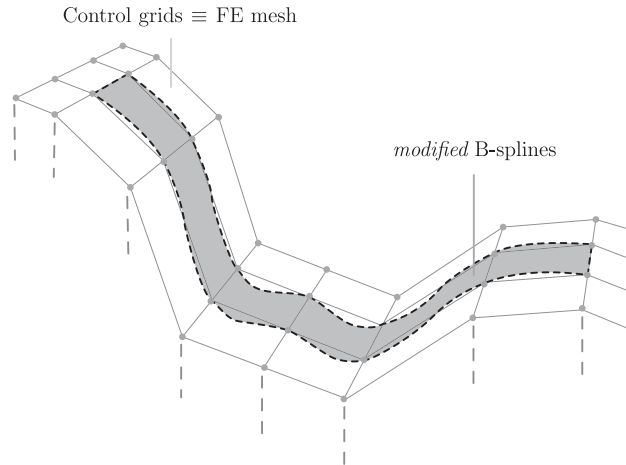


Figure 8. Part of the deformed finite element mesh (shown in Figure 7) where the contractor cube is in contact with the target plate. The modified cubic B-spline surfaces that are used for the contact surface's description are shown. The parametrization accurately interpolates the nodes of the discretized model. However, small waves are noted for abrupt curvature changes within short distances (see the middle section).

sliding are plotted with respect to its  $y$ -displacements (as indicated in Figure 7(a)). The contact forces are obtained as the sum of all reaction forces on the brick where displacements are applied, while the different curves refer to the different parametrization techniques. The form of the two curves (minimum value in the middle of the path and maximum values at both ends) is dictated by the applied boundary conditions of the plate.

The results, as illustrated in Figure 7(b), reveal that when the uniform cubic B-splines are employed the contact forces develop smoothly along the path of the contractor. In the case of the modified B-splines, the contact force curve contains oscillations. Nevertheless, the curve remains smooth and no convergence problems are noted. Moreover, the obtained results are smoother compared with the highly varying results computed with piecewise planar descriptions [12, 14]. The reason for the waviness in the force–displacement curve was already discussed in Section 3, and it is again depicted in Figure 8. The requirement of the surface to interpolate the nodes of the finite element mesh, hence its control points, leads to small waves in areas of abrupt curvature changes within short distances (middle segments of the mesh shown in Figure 8). However, in all other regions, the  $C^2$ -continuous surface remains sufficiently smooth. Finally, the difference in the obtained results in the case of the normal B-splines and the modified B-splines derives from the difference in the surfaces' expressions and the resulting difference in the computed gap function  $g_N$  (see Figure 3(b)).

## 5.2. Numerical simulation of balloon angioplasty with stenting

In the following section, a finite element model for balloon angioplasty with stenting is presented. The model is used to simulate the contact interaction between the three involved deformable bodies, i.e. the artery and the medical devices (balloon and stent). In the first paragraphs, the geometric

and constitutive models for the three bodies are described in detail. Then, the different aspects of the simulation are given such as the used techniques, the loading procedure, the chosen boundary conditions and the generated computational mesh. Finally, the most important results of the 3D non-linear analysis are presented. The scope of this example is not only to exploit the ability of the developed numerical tool to treat more complex contact problems but also to provide an insight into the interventional treatment and into the related changes in the mechanical environment of the arterial wall.

**5.2.1. Arterial model.** A realistic (patient-specific) 3D geometric model of an atherosclerotic femoral artery is considered. This, as pointed out in the Introduction, is in contrast to the vast majority of documented numerical simulations of balloon angioplasty, in which simplified cylindrical arterial models are studied. Appropriate morphological models that represent the 3D boundary surface of diseased arterial wall are pre-requisites for a meaningful computation of strain distributions under various loading conditions and are, therefore, of significant importance. The generation of the 3D artery model is based on high-resolution MRI and NURBS surface parametrizations. A detailed description of the imaging acquisition method is documented in [30]. The reconstructed model is shown in Figure 9(a).

Regardless of the type, all arteries consist of three layers (intima, media and adventitia) with different mechanical properties [31, 44, 45]. In addition, in the case of atherosclerosis, the formed plaque adds an extra degree of heterogeneity since it exhibits a different behavior compared with the non-diseased vessel wall [46–48]. Nevertheless, in a first attempt, the artery is modeled as

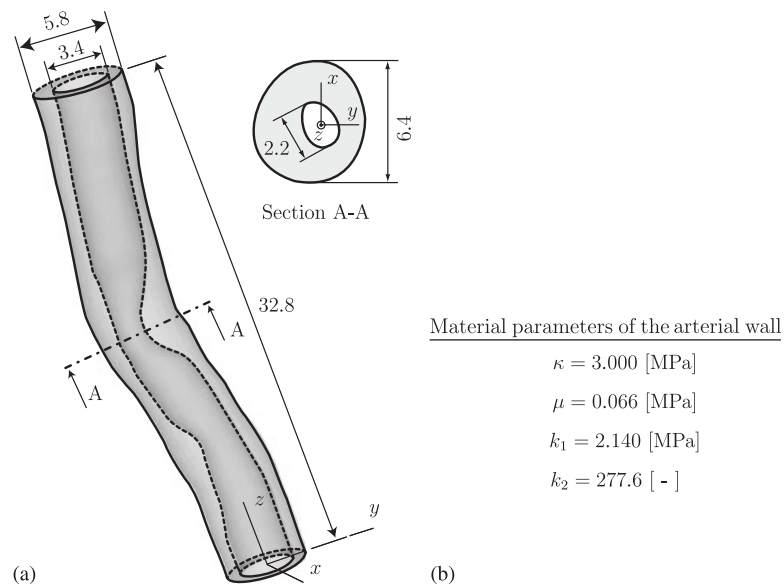


Figure 9. (a) 3D geometrical model of a highly atherosclerotic femoral artery re-constructed on the basis of hrMRI (dimensions in mm). The table summarizes the artery's material parameters determined through data fitting of uniaxial extension tests performed on arterial strips that are cut out from the circumferential and the axial directions of 11 human femoral arteries (b).

a homogeneous material. This simplification does not affect in any way the study of the contact interactions and restricts only the biological interpretation of the results.

Arterial walls are highly anisotropic due to the organized arrangement of the load-carrying (collagen fibrils) components [49]. However, there are many isotropic strain–energy functions used in practice to characterize the mechanical response of the arterial walls. The one chosen for this example is a rubber-like potential, similar to the one documented in [50]. This model is able to describe the typical stiffening effect of arteries in the high-pressure domain. The decoupled form of the strain–energy function  $\Psi$  is

$$\Psi = U(J) + \bar{\Psi}(\bar{I}_1) \quad (16)$$

where  $U$  is a purely volumetric contribution, and  $\bar{\Psi}$  is a purely isochoric contribution to the strain energy. For the volumetric part, the strictly convex function  $U = \kappa(J - 1)^2/2$  is considered, where  $\kappa$  is the bulk modulus and  $J = \det \mathbf{F} > 0$  is the local volume ratio. The bulk modulus  $\kappa$  serves as a user-specified penalty parameter chosen from numerical experiments so that the requirement of incompressibility ( $J = 1$ ) is satisfied. The isochoric part  $\bar{\Psi}$  of the strain–energy function  $\Psi$  is

$$\bar{\Psi} = \frac{\mu}{2}(\bar{I}_1 - 3) + \frac{k_1}{2k_2} \{ \exp[k_2(\bar{I}_1 - 3)^2] - 1 \} \quad (17)$$

where  $\mu > 0$  and  $k_1 > 0$  are material parameters with the dimensions of stress,  $k_2$  is a dimensionless parameter and  $\bar{I}$  is the first invariant of  $\bar{\mathbf{C}}$ , as introduced in the previous example.

The passive, quasi-static stretch–stress response of the femoral artery, and consequently the material parameters mentioned above, is determined through mechanical tests, performed on a computer-controlled, high-precision tensile machine. The procedure is documented in, for example, [48]. Briefly, uniaxial tests are performed on axial and circumferential strips extracted from the three layers (adventitia, media and intima) of 11 femoral arteries, which have undergone *in vitro* balloon angioplasty. All tissue samples are stretched far beyond the physiological loading domain up to failure in order to capture the range of deformations induced by the stent. The above constitutive model is fitted to the (averaged) behavior of all three layers in both artery directions. A least-square fitting algorithm provides the values for the three parameters, which are summarized in Figure 9(b).

**5.2.2. Stent model.** In the presented simulation, one type of stent design is investigated. It is based on the previously commercially available Palmaz–Schatz<sup>TM</sup> (Johnson & Johnson) balloon-expandable stent. The chosen stent geometry is traced from photographs, and in its undeformed configuration, it resembles a tube with rectangular slots (see Figure 10(a)).

The 3D computer model of the stent is generated by means of a parametrization algorithm. The developed technique is able to describe the stent's overall dimensions as well as the geometry of its cells. In addition, the design parameters of the algorithm are stent length, unexpanded diameter, number of its cells in the axial and circumferential directions and thickness of the strut that is considered to have a cylindrical cross section. The algorithm can provide the finite element mesh for the parametrized stent. The advantage of such a method is the automated and fast generation of different stent designs. A systematic parametric study (as the one presented in [23]) could lead to optimal, patient-tailored stent designs. In this study, two stent designs are investigated. Their geometrical models are identical, but the thickness of their struts differs. The chosen stent parameters are summarized in Figure 10(b).

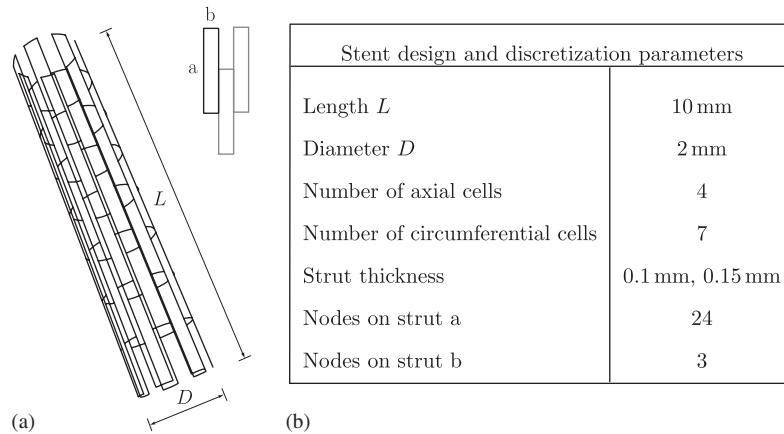


Figure 10. Model of a Palmaz-Schatz™ balloon-expandable stent: (a) undeformed configuration of the stent and (b) design and discretization parameters used for the automatic generation of the geometry and computational mesh of the stent.

The material of the stents is considered to be of stainless steel. For the elastic domain of the material, a neo-Hookean model is used, while its inelastic constitutive response is described through a von Mises–Hill plasticity model with linear isotropic hardening. Young’s modulus is chosen to be  $E = 2.01 \times 10^5 \text{ N/mm}^2$  and the Poisson ratio is  $\nu = 0.3$ . The parameters  $\sigma_y = 3.0 \times 10^2 \text{ N/mm}^2$  and  $H_{\text{iso}} = 2.0 \times 10^3 \text{ N/mm}^2$  are selected for the yield stress and the hardening modulus, respectively.

**5.2.3. Balloon model.** We consider a Grüntzig-type balloon catheter [51]. This specific type is widely used in clinical practice and therefore selected. The reference configuration of the balloon is modeled as a cylindrical tube with external diameter  $D_e = 2.0 \text{ mm}$ , wall thickness  $H = 0.2 \text{ mm}$  and length  $L = 12.0 \text{ mm}$ , as shown in Figure 11(a).

The dilation of this type of balloon catheters is characterized by complex kinematics, where the unfolding process of the balloon is followed by a typically non-linear, stiffening behavior at a higher pressure level. In the present simulation, the complex unfolding process of the balloon is neglected, while a cylindrically orthotropic model is developed in order to describe the overall mechanical behavior of the balloon. This material model is described below and is based on a fiber-reinforced material, as used in [52].

Two material axes are introduced, which are oriented in circumferential and longitudinal directions. The matrix material of the balloon catheter is considered as a (soft) isotropic material. The balloon in the circumferential direction is assumed to be very soft at its initial configuration and particularly stiff after a predefined stretch limit, whereas in the longitudinal direction it is assumed to be already stiff at its reference configuration. This ‘artificial’ setting, as shown next, is able to satisfyingly model the physical behavior of balloon catheters.

An additive split of the isochoric strain–energy function  $\bar{\Psi}$  is suggested. Hence,  $\bar{\Psi}$  consists of a part  $\bar{\Psi}_{\text{iso}}$  associated with isotropic deformations of the matrix material and a part  $\bar{\Psi}_{\text{aniso}}$  associated with anisotropic deformations. The two-term potential can then be expressed as

$$\bar{\Psi}(\bar{\mathbf{C}}, \mathbf{a}_{01}, \mathbf{a}_{02}) = \bar{\Psi}_{\text{iso}}(\bar{\mathbf{C}}) + \bar{\Psi}_{\text{aniso}}(\bar{\mathbf{C}}, \mathbf{a}_{01}, \mathbf{a}_{02}) \quad (18)$$

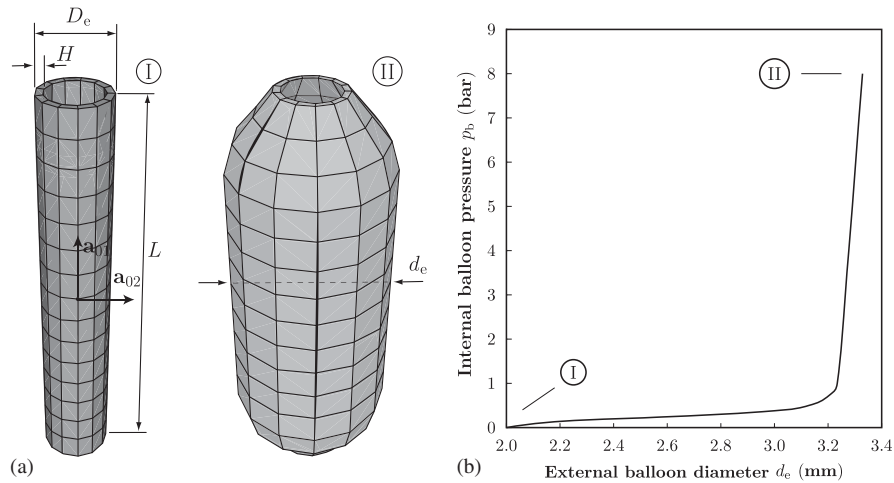


Figure 11. Finite element simulation of the dilation of a Grüntzig-type balloon catheter: (a) geometry and computational mesh of the undeformed ① and deformed ② configurations of the balloon and (b) applied internal balloon pressure  $p_b$  versus external balloon diameter  $d_e$ . Initially, the balloon expands quickly and only a low internal pressure is needed for its deformation. As the pressure exceeds approximately 1 bar, the balloon stiffens and deforms only slightly.

where  $\mathbf{a}_{0i}$ ,  $i = 1, 2$ , are the reference unit directional vectors that characterize the material axes of the orthotropic model (see Figure 11(a)).

By introducing the structure tensors  $\mathbf{A}_i$ ,  $i = 1, 2$ , defined as the tensor products  $\mathbf{a}_{0i} \otimes \mathbf{a}_{0i}$ ,  $i = 1, 2$ , we may express [52]

$$\bar{\Psi}(\bar{\mathbf{C}}, \mathbf{A}_1, \mathbf{A}_2) = \bar{\Psi}_{\text{iso}}(\bar{I}_1) + \bar{\Psi}_{\text{aniso}}(\bar{I}_4, \bar{I}_6) \tag{19}$$

with

$$\bar{I}_1 = \text{tr} \bar{\mathbf{C}}, \quad \bar{I}_4 = \bar{\mathbf{C}} : \mathbf{A}_1, \quad \bar{I}_6 = \bar{\mathbf{C}} : \mathbf{A}_2 \tag{20}$$

The invariants  $\bar{I}_4$  and  $\bar{I}_6$  are the squares of the stretches in the directions of  $\mathbf{a}_{01}$  and  $\mathbf{a}_{02}$ , respectively, and have, therefore, a clear physical interpretation. From the above equation, it is obvious that anisotropy arises only through  $\bar{I}_4$  and  $\bar{I}_6$ .

The isotropic response of the matrix material is determined through a neo-Hookean model of the form  $\bar{\Psi}_{\text{iso}} = \mu(\bar{I}_1 - 3)/2$ , where  $\mu > 0$  is a stress-like material parameter. For the description of the anisotropic part of the strain–energy function, the following equation is proposed:

$$\bar{\Psi}_{\text{aniso}}(\bar{I}_4, \bar{I}_6) = \sum_{i=4,6} \frac{d_{1,i}}{n} (\bar{I}_i - d_{2,i})^n \tag{21}$$

The parameters  $n$  and  $d_{2,i}$ ,  $i = 4, 6$ , are dimensionless, whereas  $d_{1,i}$ ,  $i = 4, 6$ , have dimensions of stress. The stiffness in each direction is described by  $d_{1,i}$ , whereas  $d_{2,i}$  defines the initial point of storage of strain energy or, in other words, the initiation of the balloon’s stiffening behavior.

In the present simulation, the chosen values for the three parameters mentioned above do not derive from a fitting algorithm of experimentally observed pressure–diameter responses of

Grüntzig-type balloon catheters. The values are chosen with respect to (i) the typically observed behavior of balloon catheters and (ii) the requirements of the problem in hand. Balloon catheters are axially stiff in their reference configuration, which can be accounted for by choosing a value  $d_{2,4} = 1$ . The operational diameter of the balloon catheter should be taken into account. The fully expanded diameter of the balloon is chosen to be equal to the diameter of the healthy part of the artery, hence approximately 3.5 mm. This implies a desired total circumferential stretch of 1.7 and, consequently, leads to  $d_{2,6} = 2.25$  (activation of circumferential stiffening at a stretch of 1.5). For both directions, the values  $d_1 = 500$  and  $n = 3$  are chosen, and for the neo-Hookean model, the value  $\mu = 100 \text{ N/mm}^2$  is used.

The results of a finite element analysis of the dilation of a balloon catheter, based on the model and the parameters given above, are shown in Figure 11. The reference and the deformed configuration, and the applied internal balloon pressure *versus* the external balloon diameter are given. As can be seen in Figure 11(a), with the exception of the boundaries, the inflated balloon has a similar cylindrical shape as the balloon in its initial configuration, which is close to the behavior of Grüntzig-type balloon catheters. In Figure 11(b), it is shown that during inflation the external balloon diameter  $d_e$  increases rapidly at the beginning and then, between balloon pressures  $p_b = 1$  and 6 bar, the balloon expands only slightly with inflation pressure, exposing a strong non-linear behavior. These results qualitatively agree with the experimental study published in [53]. Note that this peculiar mechanical response could not be obtained by means of isotropic material models.

**5.2.4. Contact interactions.** In the numerical modeling of stenting, three surfaces may come into contact and have to be specified as contact pairs. The involved pairs are (i) stent–balloon, (ii) stent–artery and (iii) artery–balloon. In all three cases, the first body is considered as the contractor body and the second as the target. Following the node-to-surface approach, the contractor surfaces are described by contractor points, which are the nodes of the finite element mesh located on the contacting surface. The target surfaces are discretized by means of the uniform cubic B-spline surfaces, as described in Section 3.

Although the contact approach could be extended to capture frictional behavior, the simulation is carried out without friction since reliable coefficients describing the frictional behavior between the intimal surface and the medical devices are not yet available.

**5.2.5. Finite element discretization.** One of the important aspects of simulating balloon angioplasty with stenting is the discretization of the involved geometric models of the artery, the balloon and the stent. Especially in the case where multiple contact problems are considered, fine meshes could lead to computationally expensive and prohibiting computations. Nevertheless, the chosen number of elements and nodes should always lead to numerically stable and reliable solutions. As mentioned in Section 3, cubic B-splines depend upon structured surface grids of  $4 \times 4$  nodes. This requirement leads to the discretization of every target surface by means of structured hexahedral elements.

As can be seen from Figure 9, the morphology of the investigated arterial specimen is complex. The artery is heavily sclerotic (small lumen), and for this reason, the thickness and the curvature of the arterial wall vary significantly along the axis of the artery. It is, therefore, clear that the generation of a computational mesh consisting exclusively of hexahedral elements is a challenging task. The mesh generation toolkit CUBIT [54] addresses the problem successfully. The obtained mesh consists of 4215 eight-node isoparametric hexahedral elements.

The generation of the computational meshes for the balloon and the stent requires less amount of effort since their geometry does not present the same complexity. The design of the stent implies the use of two-node 3D frame elements. The mesh in this case is generated automatically through the algorithm mentioned previously, which also provides the stent's overall 3D geometry model. The parameters defining the number of nodes of each strut are given in Figure 10(b). The mesh of the stent consists of 525 nodes, each one has six degrees of freedom. The geometrical model of the balloon catheter, as in the case of the artery, is discretized by means of 195 eight-node isoparametric hexahedral elements.

*5.2.6. Boundary conditions.* The geometry of the three bodies refers to a Cartesian coordinate system, as shown in Figure 9(a). In order to avoid rigid-body motions and to construct a good-conditioned system of equations, appropriate boundary conditions have to be applied. The boundary conditions chosen in this case are as follows: (i) the end faces of the balloon and the artery are bounded in all three directions; (ii) the  $y$ - and  $z$ -displacements of a node of the stent located on its middle plane are fixed, allowing the radial expansion of the stent but not its rigid motion.

*5.2.7. Loading procedure.* In order to simulate the physiological state of the artery, a displacement-controlled axial pre-stretch of 1.2 is applied at all nodes located on the end faces of the artery. At the end of this loading, the displacement boundary conditions are replaced by equivalent reaction forces. The mean arterial pressure of 100 mmHg (13.3 kPa) is not taken into consideration in the simulation, since the loads deriving from the contact interaction of the three bodies are much higher (as shown in the following section).

In a clinical situation, the artery, the stent and the balloon catheter will deform during the insertion process, especially for the tortuous lumen investigated. However, the simulation of this process is associated with high computational cost. Hence, we have chosen a strategy where the undeformed balloon catheter and stent are placed in the lumen with an overlap. Then, in a few load steps, the penalty parameter, which enforces the contact constraint for all contact pairs, is gradually increased from zero to a desired value of 0.5 N/mm. This strategy aligns the balloon and the stent with the arterial inner surface in a numerically efficient way.

Next, the expansion of the balloon–stent–artery system is simulated. This is done by deformation-dependent pressure loads, which are applied on the inner surface of the balloon. As the inner pressure increases, the balloon catheter comes into contact with the stent, and after a further pressure increase both medical devices come into contact with the artery leading to the desired increase in the internal diameter of the arterial wall. Finally, after full expansion of the balloon at an inner pressure of approximately 8 bar, the pressure loads are gradually removed, and only the stent remains in contact with the artery.

*5.2.8. Results.* In this section, the numerical outcome of the angioplasty simulation with stenting is presented. We introduce specific indicators with the aim of quantifying the changes in the mechanical environment and the lumen area of the artery. In addition, a comparison between the two stent designs is provided, emphasizing their merits, advantages and disadvantages and providing the basis for parametric analysis and assessment of different stents. The presented results provide evidence of the ability and effectiveness of the developed computational tools to treat challenging 3D contact problems such as the 3D simulation of balloon angioplasty with stenting.

A meaningful measure characterizing the success rate of the discussed medical treatment is the change in the lumen area during and after balloon angioplasty with stenting. We denote this

measure as **Lumen Gain** and is expressed through the factor LG, which was introduced in [23], and defined as

$$LG = \frac{A_{1,cur}}{A_{1,ref}} - 1 \quad (22)$$

where  $A_{1,ref}$  is the area of the smallest cross section of the inner arterial wall before stenting, and  $A_{1,cur}$  is the related current area of the cross section at the same location.

Figure 12 shows the change in LG at  $z=17.5$  mm (location of the narrowest lumen area, see Section A–A in Figure 9) with respect to the internal balloon pressure  $p_b$ . The inflation and deflation paths, when both stents (stent<sub>I</sub> and stent<sub>II</sub>) are used, are illustrated by dashed lines of different intensity. As can be seen from Figure 12, stent<sub>I</sub> leads to  $LG=0.81$  when the balloon is fully inflated ( $p_b=8$  bar), and to  $LG=0.24$  when the balloon is removed ( $p_b=0$  bar). Similarly, when the simulation is performed with stent<sub>II</sub>, the values  $LG=0.67$  and  $0.40$  are obtained. These results clearly point out that at the end of the balloon inflation, stent<sub>I</sub> is wider expanded, providing a higher LG value. Nevertheless, as the balloon is gradually deflated and finally removed, stent<sub>II</sub> with thicker struts leads to an almost 70% wider lumen in comparison with stent<sub>I</sub>, indicating a more successful outcome of the treatment, as far as the lumen area is concerned. The edges in the  $LG-p_b$  curves at the points  $p_b=1.2$  and 2.8 bar for stent<sub>I</sub> and stent<sub>II</sub>, respectively, correspond to the elastic limit of the two stents.

Similar results can be seen in Figure 13, where the lumen area  $A_1$  is plotted along the  $z$ -axis (the balloon catheter and the stent are located between  $z=13.4$  and 21.4 mm). The three curves in each plot refer to the reference lumen area, the lumen area at full balloon inflation ( $p_b=8$  bar) and after balloon removal ( $p_b=0$  bar). The total lumen gain at the end of the procedure is represented

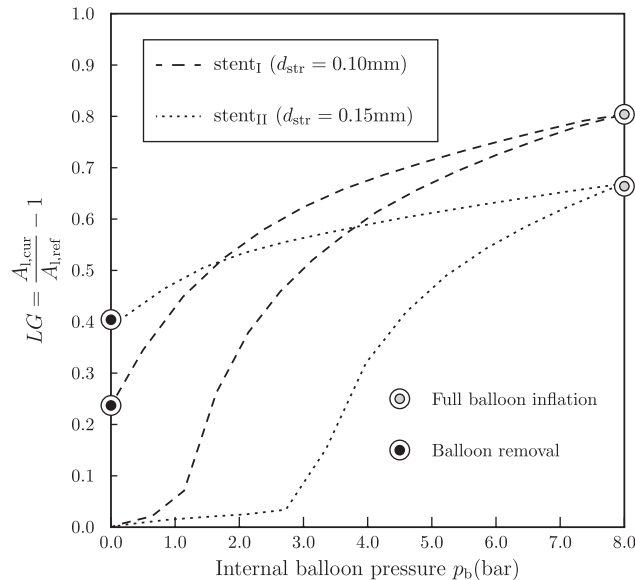


Figure 12. Lumen Gain factor (LG) versus internal balloon pressure  $p_b$  at the most stenotic section of the arterial wall, at Section A–A (compare with Figure 9). The two curves indicate the change in LG along the inflation and deflation paths of the balloon for both stent designs (stent<sub>I</sub> and stent<sub>II</sub>).

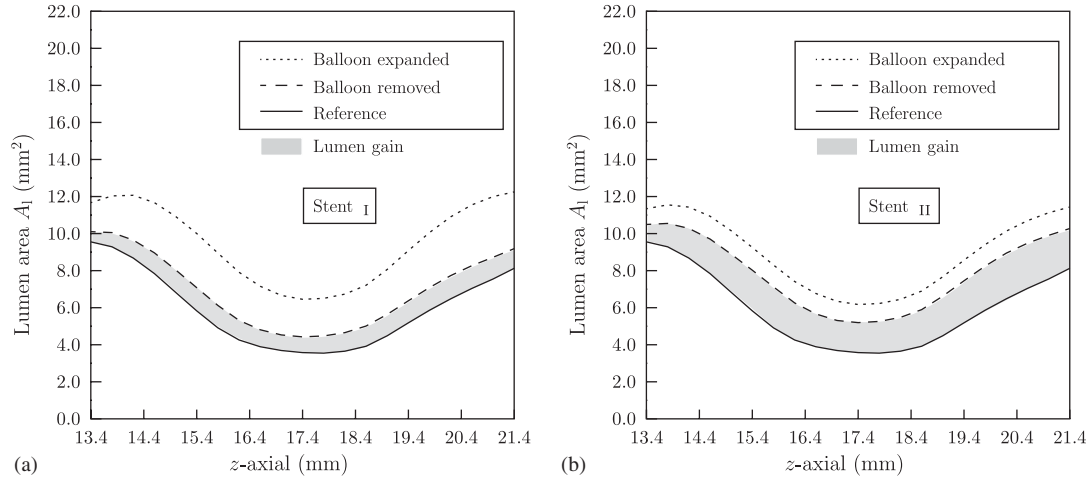


Figure 13. Lumen area  $A_l$  at the reference configuration, after full balloon expansion and after balloon removal plotted along the  $z$ -axis (see Figure 9) where the balloon and the stent are located. The results obtained for the two different stents (stent<sub>I</sub> and stent<sub>II</sub>) are shown in (a) and (b), respectively: (a) strut diameter  $d_{\text{str}}=0.10$  mm and (b) strut diameter  $d_{\text{str}}=0.15$  mm.

by the gray area. An immediate comparison between the two figures indicates that both stents provide a successful outcome, but stent<sub>I</sub> leads to a smaller lumen area throughout the stenotic part of the femoral artery under investigation. Comparable results linking the stent strut thickness and the lumen gain are also reported in the numerical study [23]. Finally, from Figure 13 one can derive the conclusion that the profile of the inner arterial wall remains almost unaltered throughout the procedure.

One of the most important drawbacks of angioplasty is the vascular damage caused by the stent struts. As documented in [55], elevated pressures around the struts may lead to growth of the artery tissue and to a decreased success rate of the angioplasty treatment due to restenosis. In addition, References [56, 57] conclude that permanent, non-physiological strains, generated in the arterial wall during and after the expansion of the stent, may also lead to cellular proliferation and, finally, to restenosis. All the above imply that the optimization of stenting and the stent design is not a one-parameter problem (for example, maximization of lumen area). Therefore, additional indicators, which allow the quantification of the changes in the mechanical environment of the artery, should be introduced. Taking the above into consideration, a deeper insight of the generated pressure and strain fields of the arterial wall can be achieved.

Figures 14 and 15 illustrates the numerical results of the performed simulations in the form of the contact pressure and the strain distribution, respectively. In particular, Figure 14 illustrates the contact pressure  $p_c$  that acts on the stenotic inner arterial wall for both cases stent<sub>I</sub> and stent<sub>II</sub> after complete deflation and removal of the balloon catheter ( $p_b=0$  bar). The contact pressure is computed for each finite element facet  $\mathbf{q}_j$  of the inner surface of the artery through

$$p_{c,j} = \frac{1}{4} \frac{\sum_{i=1}^4 F_{i,j}}{A_j} \quad (23)$$

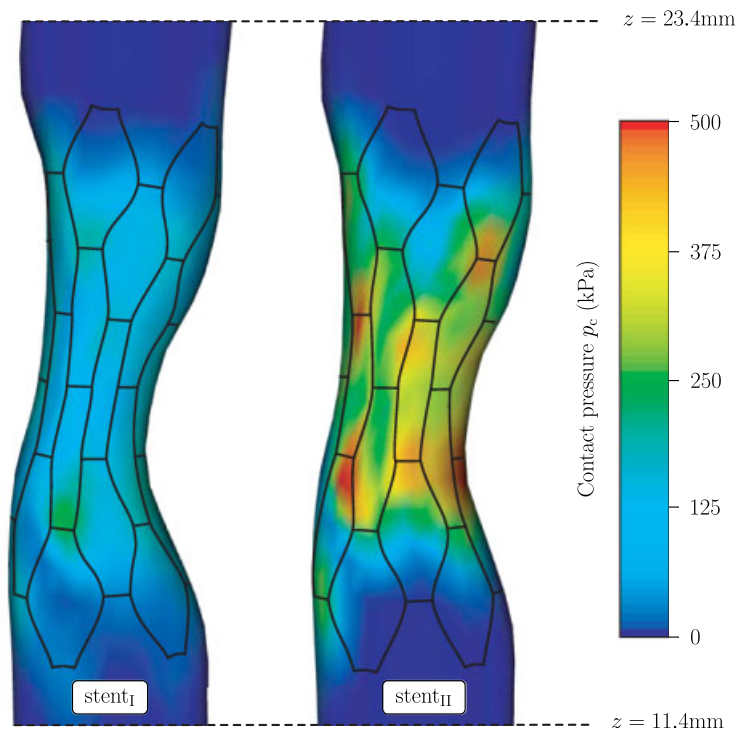


Figure 14. Distribution of the contact pressure  $p_c$  acting on the stenotic inner arterial wall through the stent struts after removal of the balloon for both cases  $\text{stent}_I$  and  $\text{stent}_{II}$ .

where  $F_{i,j}$  denote the reaction forces at the four nodes of each facet  $\mathbf{q}_j$ , and  $A_j$  is the area of the facet. A comparison of the two figures (Figures 14(a) and (b)) indicates, as expected, that the generated contact pressure in the case of the stiffer  $\text{stent}_{II}$  is approximately two times higher compared with that in  $\text{stent}_I$ , while the pressure field retains almost the same pattern. Interestingly, the position of the highest pressure is located around the horizontally positioned struts of the stents.

Another possible information that could be provided by the performed numerical simulations, and that possibly characterizes the short- and long-term mechanical changes in the arterial wall, are the stresses within the stenotic arterial wall. In this study, however, the tissue is modeled as a homogeneous and isotropic material (see, Section 5.2.1). This simplification does not allow a physical interpretation of the stresses. A more reliable and informative measure is the strain.

Figure 15 shows the distribution of the principal Euler–Almansi strains, say  $e_1, e_2, e_3$ , at the current configuration of the most stenotic section of the femoral artery ( $z = 17.5 \text{ mm}$ ), at (a) full expansion of the angioplasty balloon and (b) after removal. The results for both  $\text{stent}_I$  and  $\text{stent}_{II}$  are graphically illustrated. The strains reported at full balloon inflation depict the short-term changes in the mechanical environment of the artery due to stenting, whereas the strains after removal of the balloon indicate the more important (for the outcome of the medical procedure) long-term evolution of the loading field.

Since the circumferential direction is the main loading direction in balloon angioplasty with stenting (due to the radial expansion of the balloon and stent), it can be concluded that the principal

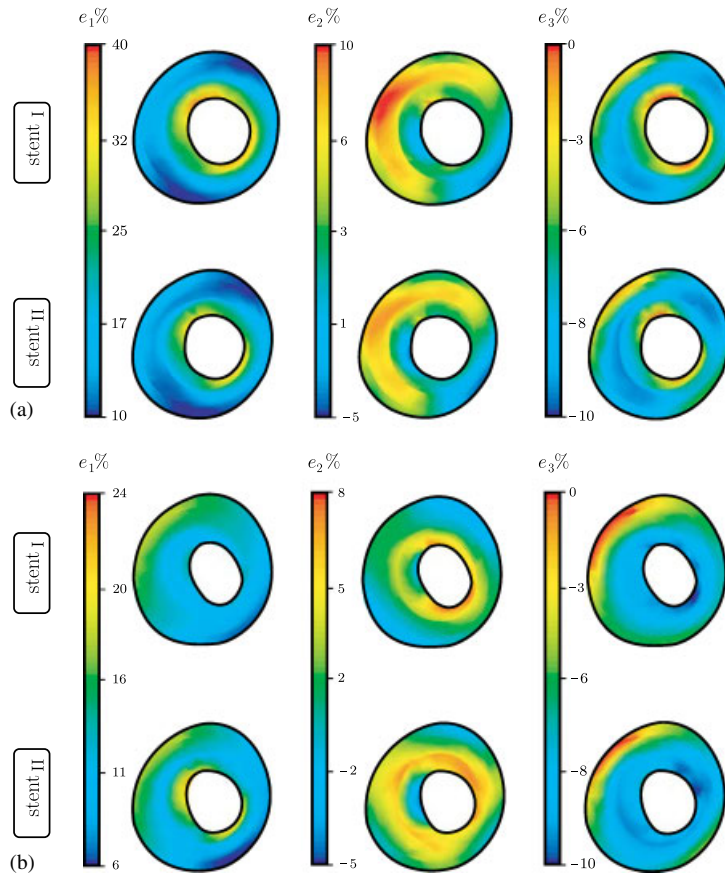


Figure 15. Comparison of the induced Euler–Almansi principal strain fields due to stenting (stent<sub>I</sub> and stent<sub>II</sub>) at the deformed configuration of the most stenotic section of the arterial wall ( $z = 17.5$  mm). The strains are plotted at two characteristic stages of the procedure: (a) at full balloon inflation ( $p_b = 8.0$  bar) and (b) after balloon removal ( $p_b = 0$  bar).

axis 1 (where the highest strains are reported—40%) is the circumferential direction. The axial displacement loads applied at the end faces of the artery, representing the physical pre-stretch of the artery tissue (as documented in Section 5.2.7), leads to approximately 10% axial stretch of the middle, highly curved part of the arterial wall. This value is comparable to the maximum computed value of the principal strain  $e_2$ , as shown in Figure 15(a). Hence, it can be assumed that the principal direction 2 is the axial direction. It should be mentioned that the curved geometry of the artery is responsible for the presence of tensile and compressive axial loads in the same section. Finally, we may conclude that the principal axis 3 is mainly located along the radial direction.

As mentioned previously, the thinner stent<sub>I</sub> is expanded further than stent<sub>II</sub>, since stent<sub>II</sub> is stiffer. Therefore, when the angioplasty balloon is fully inflated, the computed circumferential strains are approximately 10% higher at the inner border of the arterial wall, when stent<sub>I</sub> is used. Exactly the opposite is the case after balloon deflation (Figure 15(b)), where 10% higher circumferential strains are computed for the case of stent<sub>II</sub>. This leads to the conclusion that the non-physiological

loading applied with stent<sub>II</sub> has a more severe effect on the mechanical environment of the artery after the end of the procedure. On the other hand, with stent<sub>II</sub> a wider lumen area is achieved, as can be seen in Figure 15(b). For the principal strains  $e_2$ , similar conclusions can be drawn, although the differences in induced axial strains when stent<sub>I</sub> or stent<sub>II</sub> is used are not as profound as in the circumferential direction. Note that the tensile and compressive zones are almost concentrically distributed after balloon deflation. Finally, the principal strain field  $e_3$  preserves almost the same pattern, with the distinct difference that the removal of the balloon leads to higher negative radial strains around the inner arterial wall.

## 6. DISCUSSION AND CONCLUSION

Physical modeling and computer simulation of balloon angioplasty with stenting is an up-to-date research topic in computational biomechanics. Computational tools such as the finite element method have the potential to provide engineers and clinicians with patient-specific analysis to optimize medical devices such as stents and balloon catheters in order to improve the clinical outcome. Today, computer simulation of stent procedures is still a demanding task due to the complex material behavior of the involved components, and more importantly, due to the 3D contact interaction of the balloon, the stent and the arterial wall. Commonly, the contact surfaces are described by planar facets that may lead to non-physical oscillations of contact forces and, consequently, to an influence of the rate of convergence within a non-linear solution scheme. Hence, there is a need for more efficient and robust contact algorithms, based on higher-order surface parametrizations.

This work proposes a new 3D contact scheme that is based on  $C^2$ -continuous parametrizations, more specifically on uniform cubic B-splines. Detailed guidelines are provided for the implementation of the scheme into the open-source program FEAP [28]. The contact algorithm was successfully applied to a classical problem in contact mechanics, involving finite deformation and large sliding, and to treat the interactions that occur during the balloon–stent inflation in an atherosclerotic artery. The proposed computational model of stenting represents an advanced approach capable of gaining more insight into the interventional treatment of atherosclerotic arteries.

Among the contributions of the paper is the use of cubic B-splines with a novel polynomial function. This parametrization technique, which we called modified cubic B-splines, retains  $C^2$ -continuity. It enables the interpolation of the superficial nodes of the contacting bodies without any approximation or fitting. Thus, more accurate representations of geometries can be acquired. Moreover, the modified cubic B-splines do not require any additional computational effort. However, the new parametrization approach also reveals a drawback. In the case where the model includes abrupt curvature changes within short distances, the modified cubic B-splines generate undesirable undulations between the finite element (control) nodes. Nevertheless, the surface always remain smooth and no convergence problems occur during the numerical analyses.

Several sophisticated numerical tools including the MATHEMATICA package ACEGEN are used in order to compute contact contributions to the finite element arrays. Such tools provide differentiated (and optimized) expressions by means of stochastic evaluations. In addition, a technique is proposed in order to limit the computational cost of finding the contact partner elements for a particular slave point and to identify the contact point in terms of the surface coordinates.

For the computer simulation of the stent procedure, a human high-grade stenotic femoral artery was considered for which a complete set of geometric and mechanical data was available. Its

geometric model was reconstructed from hrMRI images, while the mechanical response of the artery wall, considered to be homogeneous, was described by an isotropic hyperelastic model able to capture the non-linear effect of artery tissues within the finite strain domain. In addition, the model considered the axial *in situ* pre-stretch of the artery. Besides the homogeneity and isotropy assumptions, the arterial model did not address vascular injuries which may occur during stent inflation. The mechanical response of the balloon catheter was described by an orthotropic model, which is (almost) non-compliant in the axial direction. The model enables very soft responses in the circumferential direction at low internal pressures, while exposing a stiffening effect at higher pressure values. The initially folded shape of the balloon was not considered. Hence, there is a need for model refinements, in particular, when clinical issues are addressed.

Finally, two stent configurations (stent<sub>I</sub> and stent<sub>II</sub>) with the same geometry but with different strut thicknesses were considered to evaluate the individual lumen gain LG and the contact forces exposed on the intimal wall along with the mechanical strains in the artery. The numerical results exhibited a larger lumen gain in the case of the thicker stent<sub>II</sub> but also higher contact pressures and higher circumferential and axial strains compared with the values obtained with stent<sub>I</sub>. This finding suggests that although stent<sub>II</sub> leads to a wider lumen, it is not necessarily the optimal solution, because mechanical changes in the artery wall might be responsible for the development of cell proliferation, restenosis and failure of the procedure. This also points to the multi-parametric nature of stent optimization procedures.

Undoubtedly, there is room for refinements in future studies. Uniform and modified cubic B-splines have inherent drawbacks (structured control mesh requirements, non-accurate model representations and localized undulations) that could be refined with more advanced parametrization techniques. On the constitutive modeling side, the heterogeneity of diseased vessel walls should be considered, as, for example, in [23]. The experimentally identified anisotropic behavior of artery tissues due to collagen reinforcement should be modeled by (more) advanced strain–energy functions, as presented in [45, 52, 58]. Despite the mentioned limitations, the proposed contact algorithm has the ability to address realistic 3D problems in biomechanics, where finite deformations and arbitrarily curved geometries are involved. A thorough biomechanical simulation on such a basis (patient-specific model, three-body contact) could serve as a foundation for realistic risk assessment and for designing intervention.

#### ACKNOWLEDGEMENTS

Special thanks go to Professor Robert L. Taylor at UC Berkeley who assisted us in the implementation of the contact algorithm into FEAP by means of numerous e-mails. The authors would also like to thank Martin Auer and Gerhard Sommer for their helpful support in providing images and material data of the femoral artery, and Michael Stadler who helped in initiating the early part of this work.

#### REFERENCES

1. Thom T *et al.* *Heart Disease and Stroke Statistics—2006 Update*, vol. 113. A Report from the American Heart Association Statistics Committee and Stroke Statistics Subcommittee, 2006.
2. Laursen TA. *Computational Contact and Impact Mechanics*. Springer: Berlin, 2002.
3. Wriggers P. *Computational Contact Mechanics*. Wiley: Chichester, 2002.
4. Glowinski R, Lions JL, Trémolierès R. *Numerical Analysis of Variational Inequalities*. North-Holland: Amsterdam, 1981.

5. Krstulović-Opara L, Wriggers P, Korelc J. Symbolically generated 3D smooth polynomial frictional contact element based on the quartic Bézier surfaces. In *CD-ROM Proceedings of the European Congress on Computational Methods in Applied Sciences and Engineering, ECCOMAS 2000*, Oñate E, Buega G, Suárez B (eds), Barcelona, Spain, 2000.
6. Padmanabhan V, Laursen TA. A framework for development of surface smoothing procedures in large deformation frictional contact analysis. *Finite Elements in Analysis and Design* 2001; **37**:173–198.
7. Pietrzak G, Curnier A. Continuum mechanics modelling and augmented Lagrangian formulation of multibody, large deformation frictional contact problems. In *Proceedings of COMPLAS*, vol. 5, Owen DR, Hinton E, Oñate E (eds). International Center for Numerical Methods in Engineering (CIMNE): Barcelona, 1997; 878–883.
8. El-Abbasi N, Meguid SA, Czekanski A. On the modelling of smooth contact surfaces using cubic splines. *International Journal for Numerical Methods in Engineering* 2001; **50**:953–967.
9. Al-Dojayli M, Meguid SA. Accurate modeling of contact using cubic splines. *Finite Elements in Analysis and Design* 2002; **38**:337–352.
10. Dalrymple T. An analytical overlay technique for describing deformable contact surfaces. In *CD-ROM Proceedings of the European Congress on Computational Methods in Applied Sciences and Engineering, ECCM 1999*, Wunderlich W (ed.). Institut für Statik, München, 1999.
11. Stadler M, Holzapfel GA, Korelc J.  $C^n$ -continuous modeling of smooth contact surfaces using NURBS and applications to 2D problems. *International Journal for Numerical Methods in Engineering* 2003; **57**:2177–2203.
12. Stadler M, Holzapfel GA. Subdivision schemes for smooth contact surfaces of arbitrary mesh topology in 3D. *International Journal for Numerical Methods in Engineering* 2004; **60**:1161–1195.
13. Catmull E, Clark J. Recursively generated B-spline surfaces on arbitrary topological meshes. *Computer Aided Design* 1978; **10**:350–355.
14. Krstulović-Opara L, Wriggers P, Korelc J. A  $C^1$ -continuous formulation for 3D finite deformation frictional contact. *Computational Mechanics* 2002; **29**:27–42.
15. Stolpmann J, Brauer H, Stracke H-J, Erbel R, Fischer A. Practicability and limitations of finite element simulation of the dilation behaviour of coronary stents. *Materialwissenschaft und Werkstofftechnik* 2003; **34**:736–745.
16. Rogers C, Tseng DY, Squire JC, Edelman ER. Balloon–artery interactions during stent placement: a finite element analysis approach to pressure, compliance and stent design as contributors to vascular injury. *Circulation Research* 1999; **84**:378–383.
17. Auricchio F, Di Loreto M, Sacco E. Finite-element analysis of a stenotic revascularization through a stent insertion. *Computer Methods in Biomechanics and Biomedical Engineering* 2001; **4**:249–264.
18. Migliavacca F, Petrini L, Massarotti P, Schievano S, Auricchio F, Dubini G. Stainless and shape memory alloy coronary stents: a computational study on the interaction with the vascular wall. *Biomechanics and Modeling in Mechanobiology* 2004; **2**:205–217.
19. Lally C, Dolan F, Prendergast PJ. Cardiovascular stent design and vessel stresses: a finite element analysis. *Journal of Biomechanics* 2005; **38**:1574–1581.
20. Wu W, Wang WQ, Yang DZ, Qi M. Stent expansion in curved vessel and their interactions: a finite element analysis. *Journal of Biomechanics* 2007; **40**:2580–2585.
21. Timmins LH, Moreno MR, Meyer CA, Criscione JC, Rachev A, Moore Jr JE. Stented artery biomechanics and device design optimization. *Medical and Biological Engineering and Computing* 2007; **45**:505–513.
22. Holzapfel GA, Stadler M, Schulze-Bauer CAJ. A layer-specific three-dimensional model for the simulation of balloon angioplasty using magnetic resonance imaging and mechanical testing. *Annals of Biomedical Engineering* 2002; **30**:753–767.
23. Holzapfel GA, Stadler M, Gasser TC. Changes in the mechanical environment of stenotic arteries during interaction with stents: computational assessment of parametric stent design. *Journal of Biomechanical Engineering* 2005; **127**:166–180.
24. Liang DK, Yang DZ, Qi M, Wang WQ. Finite element analysis of the implementation of a balloon expandable stent in a stenosed artery. *International Journal of Cardiology* 2005; **104**:314–318.
25. DeBoor C. *A Practical Guide to Splines*. Springer: Berlin, 1978.
26. Böhm W, Farin G, Kahmann J. A survey of curve and surface methods in CAGD. *Computer Aided Geometric Design* 1984; **1**:1–60.
27. Farin G. *Curves and Surfaces for Computer-aided Geometric Design*. Academic Press: San Diego, 1990.
28. Taylor RL. *FEAP—A Finite Element Analysis Program, Version 7.5 User Manual*. University of California at Berkeley, Berkeley, California, 2005.

29. Puso MA, Laursen TA. A mortar segment-to-segment frictional contact method for large deformations. *Computer Methods in Applied Mechanics and Engineering* 2004; **193**:4891–4913.
30. Auer M, Stollberger R, Regitnig P, Ebner F, Holzapfel GA. 3-D reconstruction of tissue components for atherosclerotic human arteries based on high-resolution MRI. *IEEE Transactions on Medical Imaging* 2006; **25**:345–357.
31. Holzapfel GA. Determination of material models for arterial walls from uniaxial extension tests and histological structure. *Journal of Theoretical Biology* 2006; **238**:290–302.
32. Wriggers P, Miehe C, Kleiber M, Simo JC. On the coupled thermomechanical treatment of necking problems via finite element methods. *International Journal for Numerical Methods in Engineering* 1992; **33**:869–883.
33. Laursen TA, Simo JC. A continuum-based finite element formulation for the implicit solution of multibody, large deformation frictional contact problems. *International Journal for Numerical Methods in Engineering* 1993; **36**:3451–3485.
34. *MATHEMATICA 5.1—Documentation*. Wolfram Research, Inc., 2005.
35. Puso MA, Laursen TA. A 3D smoothing method using Gregory patches. *USACM Sixth U.S. National Congress on Computational Mechanics: Abstracts*. Mechanical Engineering Department, University of Michigan, 2001.
36. Ateshian GA. A B-spline least-squares surface-fitting method for articular surfaces of diarthrodial joints. *Journal of Biomechanical Engineering* 1993; **115**:366–373.
37. Hirokawa S, Ueki T, Ohtsuki A. A new approach for surface fitting method of articular joint surfaces. *Journal of Biomechanics* 2004; **37**:1551–1559.
38. Van Ruijven LJ, Beek M, Van Eijden TMGJ. Fitting parametrized polynomials with scattered surface data. *Journal of Biomechanics* 1999; **32**:715–720.
39. Dhaher YY, Delp SL, Rymer WZ. The use of basis function in modelling joint articular surfaces: application to the knee joint. *Journal of Biomechanics* 2000; **33**:901–907.
40. Kagan P, Fischer A, Bar-Yoseph PZ. New B-spline finite element approach for geometrical design and mechanical analysis. *International Journal for Numerical Methods in Engineering* 1998; **41**:435–458.
41. Cirak F, Ortiz M. Fully  $C^1$ -conforming subdivision elements for finite deformation thin-shell analysis. *International Journal for Numerical Methods in Engineering* 2001; **51**:813–833.
42. Korelc J. Automatic generation of finite-element code by simultaneous optimization of expressions. *Theoretical Computer Science* 1997; **187**:231–248.
43. Holzapfel GA. *Non-linear Solid Mechanics. A Continuum Approach for Engineering*. Wiley: Chichester, 2000.
44. Rhodin JAG. Architecture of the vessel wall. In *Handbook of Physiology, The Cardiovascular System*, vol. 2, Bohr DF, Somlyo AD, Sparks HV (eds). American Physiological Society: Bethesda, MD, 1980; 1–31.
45. Holzapfel GA, Sommer G, Gasser CT, Regitnig P. Determination of the layer-specific mechanical properties of human coronary arteries with non-atherosclerotic intimal thickening, and related constitutive modelling. *American Journal of Physiology—Heart and Circulation Physiology* 2005; **289**:H2048–H2058.
46. Cox RH, Detweiler DK. Arterial wall properties and dietary atherosclerosis in the racing greyhound. *American Journal of Physiology* 1979; **236**:H790–H797.
47. Holzapfel GA, Schulze-Bauer CAJ, Stadler M. Mechanics of angioplasty: wall, balloon and stent. In *Mechanics in Biology*, Casey J, Bao G (eds). The American Society of Mechanical Engineers (ASME): New York, 2000; 141–156. *AMD-Vol. 242/BED-Vol. 46*.
48. Holzapfel GA, Sommer G, Regitnig P. Anisotropic mechanical properties of tissue components in human atherosclerotic plaques. *Journal of Biomechanical Engineering* 2004; **126**:657–665.
49. Cox RH. Passive mechanics and connective tissue composition of canine arteries. *American Journal of Physiology* 1978; **234**:H533–H541.
50. Delfino A, Stergiopoulos N, Moore Jr JE, Meister J-J. Residual strain effects on the stress field in a thick wall finite element model of the human carotid bifurcation. *Journal of Biomechanics* 1997; **30**:777–786.
51. Grüntzig A, Kumpe DA. Technique of percutaneous transluminal angioplasty with Grüntzig balloon catheter. *American Journal of Radiology* 1979; **132**:547–552.
52. Holzapfel GA, Gasser TC, Ogden RW. A new constitutive framework for arterial wall mechanics and a comparative study of material models. *Journal of Elasticity* 2000; **61**:1–48.
53. Olbrich T, Murray A. Assessment of computer-controlled inflation/deflation for determining the properties of PTCA balloon catheters with pressure–volume curves. *Physiological Measurement* 2001; **22**:299–308.
54. CUBIT Team. *CUBIT 10.0 User's Manual*. Sandia National Laboratories, Albuquerque, New Mexico, U.S.A., 2005.
55. König A, Schiele TM, Rieber J, Theisen K, Mudra H, Klauss V. Influence of stent design and deployment technique on neointima formation and vascular remodeling. *Zeitschrift für Kardiologie* 2002; **91**:98–102.

56. Leung DY, Glagov S, Mathews MB. Cyclic stretching stimulates synthesis of matrix components by arterial smooth muscle cells *in vitro*. *Science* 1976; **191**:475–477.
57. Wang DL, Wung BS, Shyy YJ, Lin CF, Chao YJ, Usami S, Chien S. Mechanical strain induces monocyte chemotactic protein-1 gene expression in endothelial cells. Effects of mechanical strain on monocyte adhesion to endothelial cells. *Circulation Research* 1995; **77**:294–302.
58. Gasser TC, Ogden RW, Holzapfel GA. Hyperelastic modelling of arterial layers with distributed collagen fibre orientations. *Journal of the Royal Society of Interface* 2006; **3**:15–35.